Robust Speed Control Strategy of PMSMs Using Improved Sliding-Mode Controller With New Reaching Law and Variable-Parameter Generalized Super-Twisting Observer

Yifan Xu, *Graduate Student Member, IEEE*, Bin Zhang, *Member, IEEE*, Yongting Deng, *Senior Member, IEEE*, Yuxin Kang, *Graduate Student Member, IEEE*, Xiufeng Liu, *Member, IEEE*, and Haiyang Cao, *Member, IEEE*

***Abstract*—This study presents a novel approach to enhance the speed control performance of the permanent magnet synchronous motor (PMSM) drive system by integrating a new sliding-mode reaching law (NSMRL) with a variable-parameter generalized super-twisting observer (VGSTO). The NSMRL is developed based on the terminal attractor concept and an adaptive method. It overcomes the slow convergence of the traditional exponential reaching law. The proposed sliding-mode controller consists of the NSMRL and an integral sliding-mode surface, achieving superior convergence dynamics. Besides, the adaptive function enhances fast transient response. The VGSTO addresses the traditional extended state observer's issue of limited bandwidth selection due to system stiffness, offering better observing performance without a large bandwidth. The added linear and extra terms further speed up observer convergence. The introduction of variable parameters further reduces the observation error of the observer. Experiments confirm the superiority of the proposed control strategy.**

***Index Terms*—Extended state observer (ESO), integral sliding-mode surface, new sliding-mode reaching law (NSMRL), permanent magnet synchronous motor (PMSM), sliding-mode control (SMC), variable-parameter generalized super-twisting observer (VGSTO).**

Received 11 March 2025; revised 26 May 2025; accepted 21 July 2025. Date of publication 24 July 2025; date of current version 27 August 2025. This work was supported in part by the National Nature Science Foundation of China under Grant 11973041 and Grant 12122304, in part by the Jilin Province Key R&D Plan Project under Grant 20220203036SF, and in part by the Jilin Province Science and Technology Innovation Platform Project under Grant 20230505007ZP. Recommended for publication by Associate Editor R. Kennel. *(Corresponding author: Bin Zhang.)*

Yifan Xu and Yuxin Kang are with the Changchun Institute of Optics, Fine Mechanics, and Physics, Chinese Academy of Sciences, Changchun 130033, China, and also with the University of Chinese Academy of Sciences, Beijing 100049, China (e-mail: xuyifan22@mails.ucas.ac.cn; kangyuxin22@mails.ucas.ac.cn).

Bin Zhang, Yongting Deng, and Xiufeng Liu are with the Changchun Institute of Optics, Fine Mechanics, and Physics, Chinese Academy of Sciences, Changchun 130033, China (e-mail: zhangbin@ciomp.ac.cn; dengyongting@ciomp.ac.cn; liuxiufeng20@mails.ucas.ac.cn).

Haiyang Cao is with the Ningbo Institute of Materials Technology and Engineering, Chinese Academy of Sciences, Ningbo 315201, China (e-mail: caohaiyang@nimte.ac.cn).

Color versions of one or more figures in this article are available at https://doi.org/10.1109/TPEL.2025.3592251.

Digital Object Identifier 10.1109/TPEL.2025.3592251

I. Introduction

PERMANENT magnet synchronous motors (PMSM) have many advantages, such as high dynamic performance, high power density, high torque-to-current ratio, and high efficiency. It is widely used in high-precision servo control systems, such as robots, CNC machine tools, and large-aperture telescopes[1], [2], [3]. However, the PMSM drive system is a multivariable, strongly coupled nonlinear system, and the traditional linear proportional-integral (PI) controller, although able to meet its control requirements to a certain extent, cannot satisfy the high-precision speed control performance of the PMSM when the system is affected by uncertain perturbations, such as internal parameter variations and external load torque [4]. Therefore, PMSM speed control strategies based on modern control theory, such as fuzzy control [5], auto-defect rejection control [6], neural network control [7], and sliding mode control (SMC) [8], [9], [10], have been widely studied. Among these methods, SMC has been widely used in PMSM drive systems because it does not require high accuracy of the system model and has strong robustness to external perturbations, which can effectively improve the system's immunity to disturbances [11].

However, in practical applications, the traditional SMC method has problems, such as slow convergence of the reaching law and high-frequency chattering owing to the time lag in switching the control law, which can reduce the transient response performance of the system [12]. Therefore, many scholars have proposed alternative methods to the traditional reaching law to overcome the shortcomings of traditional sliding mode control. Mishra et al. [13] added a terminal attractor to the traditional reaching law, which ensured faster convergence speed while removing the inherent sliding-mode chattering of the system. The literature [14] applied a discrete-time fractional-order terminal sliding mode variational structure to the velocity controller and experimentally verified that the method can improve the transient performance of the controlled system; however, the theoretical proof is relatively complicated. In [15], for the chattering problem of SMC, a reaching law combining the segmented function and the super-twisting algorithm was proposed, which not only effectively reduced the chattering of the system,

but also ensured faster convergence; however, it also increased the complexity of the algorithm. In the literature [16], the power term of the exponential term in the proposed novel reaching law is limited by the absolute value of the switching function, which means the reaching law can be expressed in two different forms during the convergence process. The reaching law not only effectively suppresses intrinsic sliding-mode chattering, but also accelerates the speed at which the system state reaches the sliding-mode surface.

In this study, in order to further improve the response speed of the control system, a terminal attractor is introduced into the reaching law. It replaces the isokinetic term in the traditional exponential reaching law. The design of the nonlinear exponential term ensures a faster convergence speed at each stage of the system state variables. The speed controller consists of an integral sliding-mode surface and the new sliding-mode reaching law (NSMRL). The introduction of the adaptive function further enhances the transient and steady-state performance of the system. Moreover, since the sign function in the traditional sliding-mode function is not used, the sliding-mode chattering of the system is well suppressed.

In conventional sliding-mode variable structure control, people want to ensure the system's strong robustness and stability [17]. So, the switching gain is usually set large enough to suppress system disturbance. When the system has a disturbance, the control switching gain will rise as the system disturbance increases. However, a larger switching gain will make the system generate high-frequency jitter. Moreover, the upper bound of the system disturbance is generally difficult to determine, which seriously affects the control performance of the system. Various observers have been proposed to solve this problem. Extended state observer (ESO), as a kind of observer that is widely used in the field of system disturbance observation, has many merits [18], [19]. In recent years, nonlinear disturbance observer control methods for uncertainty [20], [21] have been intensively investigated. The results show that by designing feed-forward compensating observers, uncertainty disturbances can be eliminated from the output without affecting the system's performance. Several scholars have made improvements to the traditional ESO. Literature [22] proposed a high-order nonlinear extended state observer (NESO) with continuous nonlinear terms to estimate the total disturbance and motor speed simultaneously, thereby achieving satisfactory control performance. In [23], a generalized NESO is used to optimize the dynamic properties of PMSM systems. Hou et al. [24] proposed a super-twisting extended state observer (STESO), which introduced the super-twisting concept into the traditional ESO and ultimately achieved good disturbance suppression effects.

To address the issue that the ESO cannot select an overly large observer bandwidth due to the influence of system stiffness and considerations of high-frequency noise [25], [26]. The VGSTO proposed in this study can achieve better observation performance without selecting too large an observer bandwidth. The adoption of variable parameters further improves the observation performance and anti-interference ability of the observer.

The main contributions made in this article are summarized as follows:

1) NSMRL is proposed based on the concepts of a nonlinear function, adaptive method, and terminal attractor, based on which the designed improved sliding-mode controller (ISMC) suppresses system sliding-mode chattering, while improving the system convergence speed.
2) The proposed VGSTO has a faster response speed and higher estimation accuracy than the traditional ESO. The introduction of variable parameters further enhances the observation performance of the observer further improves the observer observation performance, thereby optimizing the antidisturbance capacity of the PMSM system.
3) The robust speed control strategy (RSCS) based on the ISMC and VGSTO compositions has superior transient performance and robustness.

The rest of this article is organized as follows. The mathematical model of the PMSM is presented in Section II. Section III describes the design of the NSMRL and finite-time convergence proof. Section IV describes the design of the ISMC based on the NSMRL and integral sliding-mode surface. Section V introduces VGSTO and the proof of the overall stability of RSCS. Finally, Section VI presents the experiment. Finally, Section VII concludes this article.

II. Mathematical Model of PMSM Considering Disturbance Conditions

Neglecting the effects of core saturation, eddy currents, and hysteresis losses on the PMSM, the voltage equation of the surface-mounted PMSM in the synchronous rotating $(d-q)$ coordinate system can be expressed as

$$\begin{cases} u_d = Ri_d + L\frac{di_d}{dt} - P_n\omega_m L i_q \\ u_q = Ri_q + L\frac{di_q}{dt} + P_n\omega_m(Li_d + \varphi_f) \end{cases} \tag{1}$$

where u_d, u_q, i_d, and i_q represent the voltage and current components in the d and q axes, respectively, R represents the stator resistance, L is the stator inductance, ω_m represents the mechanical angular velocity of the rotor, P_n represents the polar logarithm, and φ_f represents the permanent magnet chain.

The kinetic model of PMSM can be described as

$$\dot{\omega}_m = \frac{K_t}{J}i_q - \frac{B}{J}\omega_m - \frac{T_L}{J} \tag{2}$$

where J is the moment of inertia, T_L is the load torque, B is the viscosity coefficient, and $K_t = \frac{3P_n\varphi_f}{2}$ is the torque constant. The dynamic model of the PMSM can be redescribed as

$$\frac{d\omega_m}{dt} = K_t i_q - B\omega_m - T_L. \tag{3}$$

Further, the kinetic (2) for PMSM can be rewritten as

$$\dot{\omega}_m = \frac{K_t}{J}i_q^{\text{ref}} + D_\omega \tag{4}$$

where i_q^{ref} denotes the q-axis reference current. D_ω is the aggregate disturbance, formulated as

$$D_\omega = \frac{Kt}{J}\left(i_q - i_q^{\text{ref}}\right) - \frac{T_L}{J} - \frac{B\omega_m}{J}. \tag{5}$$

III. Design of the NSMRL

The phase trajectory of the SMC can be divided into reaching and sliding phases. The reaching phase refers to the process in which the system converges from the initial state to the sliding-mode surface.

A. Design of the Traditional Exponential Reaching Law

The traditional exponential reaching law can be expressed as

$$\frac{ds}{dt} = -\varepsilon \mathrm{sgn}(s) - ks \tag{6}$$

where $\varepsilon \mathrm{sgn}(s)$ represents the isokinetic term; ks denotes the exponential term.

Although the reachability problem is solved by adding isokinetic terms, discontinuous isokinetic convergence terms cause high-frequency sliding-mode chattering, and a larger gain k of the exponential convergence terms further motivates the sliding-mode chattering caused by the isokinetic convergence terms while increasing the convergence speed of the system. This was analyzed as follows.

In (6), when $s > 0$ it can be obtained that

$$\frac{ds}{dt} = -\varepsilon - ks. \tag{7}$$

When $s(t) = 0$ integrating from 0 to t for (7)

$$-\int_{s(0)}^{s(t)} \frac{ds}{\varepsilon + ks} = \int_0^t dt. \tag{8}$$

The time to reach the sliding-mode surface can be calculated as

$$t = \frac{1}{k} \ln \left[1 + s(0) \frac{k}{\varepsilon} \right]. \tag{9}$$

From (9), it can be observed that the larger the value of k, the faster the system converges to the sliding-mode surface. Therefore, to obtain a faster convergence speed, the gain k of the exponential term should be increased; however, a value that is to k may result in the sliding-mode surface reaching too quickly, which may stimulate sliding-mode chattering.

B. Introduction of the Terminal Attractor

The terminal attractor model is shown

$$\frac{dx}{dt} = -x^{\frac{q}{p}} \tag{10}$$

where p and q are odd numbers greater and satisfy $p > q > 0$, and (10) can be transformed as

$$-x^{\frac{q}{p}} dt = dx. \tag{11}$$

Integrating both sides of (11) simultaneously gives

$$t_r = \frac{x(0)^{1-\frac{q}{p}}}{1 - \frac{q}{p}} \tag{12}$$

where $x(0)$ represents the initial state of the system state variable and t_r represents the time for the state variable in the terminal attractor to reach the equilibrium point from the initial state. From the proof, it can be concluded that the system state variables can converge to the equilibrium point in finite time, while the terminal attractor has the property of accelerating the convergence near the equilibrium point; thus, the introduction of the terminal attractor can make the system state converge quickly in finite time. The exponential reaching law for introducing a terminal attractor can be expressed as

$$\frac{ds}{dt} = -\alpha s^{\frac{q}{p}} - k_1 s. \tag{13}$$

Proof 1: When $s(t) = 0$ integrating (13) from 0 to t

$$-\int_{s(0)}^{s(t)} \frac{ds}{\alpha s^{\frac{q}{p}} + k_1 s} = \int_0^t dt. \tag{14}$$

The time to reach the sliding-mode surface can be calculated as

$$t_1 = \frac{p}{k_1(p-q)} \ln \left[1 + \frac{k_1 \cdot s(0)^{\frac{p-q}{p}}}{\alpha} \right]. \tag{15}$$

If the reaching law introducing a terminal attractor has the same convergence time as the conventional exponential reaching law, $t = t_1$. Combining (9) and (15) yields

$$\frac{1}{k} \ln \left[1 + s(0) \frac{k}{\varepsilon} \right] = \frac{p}{k_1(p-q)} \ln \left[1 + \frac{k_1 \cdot s(0)^{\frac{p-q}{p}}}{\alpha} \right]. \tag{16}$$

Further available

$$\frac{1}{k} = \frac{p}{k_1(p-q)} \tag{17}$$

where p and q are all satisfy $p > q > 0$

$$\frac{k_1}{k} = \frac{p}{p-q} > 1. \tag{18}$$

The coefficient of the exponential term in the reaching law is larger than that in the traditional exponential reaching law after the introduction of the terminal attractor; therefore, the terminal attractor enhances the speed of convergence of the exponential term in the reaching law.

C. Design of the NSMRL

Integrating the terminal attractor mentioned above and taking the $\mathrm{sign}(s)$ function into account, in this paper, a NSMRL is proposed based on the concept of the terminal attractor and the idea of an adaptive function

$$\frac{ds}{dt} = -k|s|^{b \cdot \mathrm{sgn}(|s|-1)} s - \alpha \{ \tanh[\lambda(|s| - a)] + 1 \} s^{\frac{q}{p}} \tag{19}$$

where $\alpha > 0$, $\lambda > 0$, $a > 0$, $p > q$, $k > 0$, $0 < b < 1$, and p, q are odd.

Proof 2: For the first term of the proposed NSMRL (19), when the state of the system is far from the sliding-mode surface, $\mathrm{sgn}(|s| - 1) = 1$, the improved nonlinear exponential term gain $k|s|^b$ greater than traditional exponential term gain k. The larger the sliding-mode function s is, the larger the gain of the exponential term is, and the sliding-mode function s rapidly approaches the sliding-mode surface owing to the larger gain of the exponential term. As the system state

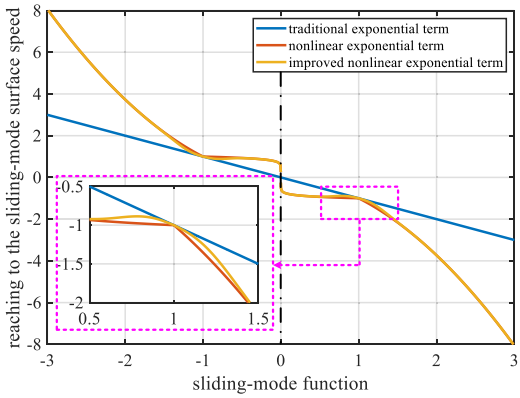

Fig. 1. Diagram of the relationship between the speed approaching the sliding-mode surface and sliding-mode function.

approaches the sliding-mode surface, the gain of the improved nonlinear exponential term $k|s|^b$ decreases as the sliding-mode function approaches the sliding-mode surface, thus avoiding the excitation of sliding-mode chattering owing to the large gain of the exponential term. When $|s| = 1$, the same gain as the conventional exponential term gain k is achieved. As the state of the system continues to approach the sliding-mode surface, the sliding-mode functions $|s| < 1$ and $\text{sgn}(|s| - 1) = -1$. At this point the gain of the improved nonlinear exponential term becomes $k|s|^{-b}$. Apparently, there is $k|s|^{-b} > 1 > k|s|^b$. Thus, the gain of the improved nonlinear exponential term is greater than or equal to that of the conventional exponential term throughout the convergence of the system state to the sliding-mode surface, where the larger the value of b, the faster the system converges.

However larger values of b speed up the convergence of the system, while at the same time, due to the introduction of the sign function. This leads to a discontinuity in the derivative of the exponential convergence term at $|s| = 1$, which in turn leads to a discontinuity in the convergence speed of the system as it converges to the sliding-mode surface, which is further exacerbated by increasing b values.

To solve this problem, an adaptive function is introduced based on the nonlinear exponential term

$$b = \beta(1 - e^{-\chi(|s|-1)^2}) \tag{20}$$

where $\chi > 0$ and $0 < \beta < 1$.

Proof 3: According to the first term in (19), when $s > 0$ and the state variable is approaching $s = 1$, due to the existence of the switching function, there will be situations of $ks^{(1-b)}$ and $ks^{(1+b)}$ on both sides of $s = 1$. If b is set as a constant, it will lead to the problem of discontinuous. However, when the adaptive function (20) is introduced, it ensures that $b = 0$ when $s = 1$. Based on ensuring continuous switching, this makes the switching of the state variable smoother when $s = 1$.

For k taking the value of 1, $\beta = 0.1$, and $\chi = 30$. The velocity at which the system converges to the sliding-mode surface versus the sliding-mode functions for the three index terms is shown in Fig. 1. The lines of three colors, respectively, represent the exponential term of the traditional exponential reaching law in (6), the nonlinear exponential term: The first term in (19), and the improved nonlinear exponential term: the first term in (19) with (20).

As mentioned previously, the value of b should not be too large, as it affects the convergence speed of the system to some extent. The second term in NSMRL (14) addresses this problem by proposing an adaptive function that ensures that the system achieves a faster convergence rate when moving away from the sliding-mode surface. The second term of NSMRL achieves a smaller switching gain to avoid overshooting the system response.

In summary, the convergence speed of NSMRL is always higher than that of the conventional exponential reaching law in the convergence stage. The introduction of the terminal attractor suppressed the sliding-mode chattering of the system, while improving the convergence speed. In addition, the introduction of the adaptive function accelerated the convergence speed of the system and suppressed sliding-mode chattering caused by the switching term to a certain extent.

Proof 4: The time required for the conventional reaching law to converge to the sliding-mode surface is

$$t_{\text{TSMC}} = \int_0^{s(0)} \frac{ds}{\varepsilon + ks} = \int_1^{s(0)} \frac{ds}{\varepsilon + ks} + \int_0^1 \frac{ds}{\varepsilon + ks}. \tag{21}$$

The upper bound on the time required for the ARL to reach the sliding-mode surface proposed in this article is:

$$t_{ARL} < \int_1^{s(0)} \frac{ds}{\alpha s^{\frac{q_s}{p_s}} + \beta s^{1+b}} + \int_0^1 \frac{ds}{\alpha s^{\frac{q_s}{p_s}} + \beta s^{1-b}} \tag{22}$$

because of

$$\int_1^{s(0)} \frac{ds}{\alpha s^{\frac{q_s}{p_s}} + \beta s^{1+b}} < \int_1^{s(0)} \frac{ds}{\varepsilon + ks} \tag{23}$$

$$\int_0^1 \frac{ds}{\alpha s^{\frac{q_s}{p_s}} + \beta s^{1-b}} < \int_0^1 \frac{ds}{\varepsilon + ks}. \tag{24}$$

Then, we have

$$t_{\text{ARL}} < t_{\text{TSMC}}. \tag{25}$$

Therefore, the NRL proposed in this article has a faster convergence rate than the traditional reaching law.

IV. Design of the ISMC

The design of the ISMC is based on the above-mentioned NMRL and the integral sliding mode surface. First, the velocity error x_1 is defined as

$$x_1 = \omega_m^{\text{ref}} - \omega_m \tag{26}$$

where ω_m^{ref} is the given mechanical angular velocity of the rotor, which is obtained by combining (4) and deriving for x_1

$$\dot{x}_1 = -\dot{\omega}_m = -\frac{K_t}{J} i_q^{\text{ref}} - D_\omega. \tag{27}$$

In the design of a conventional sliding-mode surface, introducing the differential component of the velocity error usually leads to high-frequency noise. At the same time, to further improve the speed of approaching the sliding-mode surface, in this study, according to the [27], the integral quantity x_2 of the

velocity error is introduced in the design of the sliding-mode surface as follows:

$$x_2 = \int_0^t x_1 dt = \int_0^t (\omega_m^{ref} - \omega_m) dt. \tag{28}$$

Then, the integral sliding-mode surface s is designed as follows:

$$s = x_1 + cx_2 \tag{29}$$

where $c > 0$.

Proof 5: The integral sliding-mode exhibits significant advantages in terms of approaching speed and chattering suppression.

Advantages in chatter suppression: The integral sliding-mode transfers the discontinuous control action from the actual control path to the internal dynamic process. The equivalent control is obtained by means of $c\dot{x}_1 + x_1 = s$. After redesigning the switching function, the actual control path remains continuous, thus avoiding high-frequency chattering.

Advantages in approaching speed: The integral sliding-mode enables the system to enter the sliding-mode at the initial moment. By constructing the switching function $s = s_0(x) + z$ and making z satisfy $\dot{z} = -\frac{\partial s_0}{\partial x}(f(x) + B(x)u_0(x))$ and $z(0) = -s_0(x(0))$, it ensures that $s(0) = 0$. This effectively avoids the non-robustness problem during the approaching phase and can quickly converge to the desired state.

By substituting $s = 0$ in (29), the derivation of (29) can be obtained as follows:

$$\dot{x}_1 = -cx_2. \tag{30}$$

From (30), we can solve for $x_1(t) = x_1(0)\mathrm{e}^{-ct}$, which shows that the velocity error tends to zero exponentially with the time constant c. Therefore, the dynamic characteristics of the sliding phase of the system can be expressed by the coefficient c. To design the ISMC, by combining (14), (27), and (29), we obtain

$$\begin{aligned} -\frac{K_t}{J} i_q^{ref} - D_\omega + cx_1 = & -\alpha \left\{ \tanh\left[\lambda\left(|s| - a\right) + 1\right] \right\} s^{\frac{q}{p}} \\ & - k|s|^{b \cdot \mathrm{sgn}(|s|-1)} s. \end{aligned} \tag{31}$$

Further, it follows from (31) that:

$$\begin{aligned} i_q^{ref} = \frac{J}{K_t}(cx_1 + \alpha \left\{ \tanh\left[\lambda\left(|s| - a\right)\right] + 1 \right\} s^{\frac{q}{p}} \\ + k|s|^{b \cdot \mathrm{sgn}(|s|-1)} s - D_\omega). \end{aligned} \tag{32}$$

The block diagram of the ISMC structure is shown in Fig. 2.

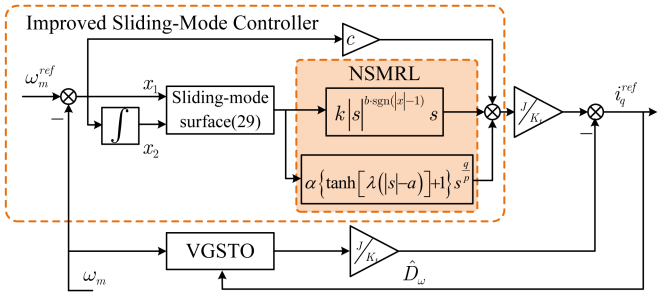

Fig. 2. Structural diagram of the ISMC.

V. VGSTO Design and Stability Demonstration

In practice, the D_ω system is usually difficult to obtain because of uncertain perturbations, such as internal parameter variations and external load torque. Therefore, the observers must be designed to estimate them appropriately and compensate for them back into the speed controller.

A. Design of the Generalized Super-Twisting Observer (GSTO)

To further improve the system's anti-interference performance, a disturbance observer is designed to observe the system's aggregate disturbance D_ω. In response because conventional ESO is not able to select an observer bandwidth that is too large because of the limitation of the system stiffness; thus, it is not possible to obtain a better observation performance. GSTO solves the above problem, and the introduction of linear and extra terms further improves the convergence speed.

According to (27), GSTO can be designed as

$$\begin{cases} \dot{\hat{\omega}}_m = -l_1\phi_1(e_1) + \frac{K_t}{J} i_q^{ref} + D_\omega \\ \dot{\hat{D}}_\omega = -l_2\phi_2(e_1) \end{cases} \tag{33}$$

where $e_1 = \omega_m - \hat{\omega}_m$, $e_2 = D_\omega - \hat{D}_\omega$, $\hat{\omega}_m$, and $\hat{D}_\omega$ is the observed value of the observer. The bandwidth parameterization strategy is adopted to select the observer gain, from which it is derived that

$$\begin{cases} l_1 = 2\omega_c \\ l_2 = {\omega_c}^2 \end{cases} \tag{34}$$

$$\begin{cases} \phi_1(e_1) = \mu_1 |e_1|^{\frac{1}{2}} \mathrm{sgn}(e_1) + \mu_2 e_1 \\ \phi_2(e_1) = \frac{{\mu_1}^2}{2} \mathrm{sgn}(e_1) + \frac{3}{2}\mu_1\mu_2 |e_1|^{\frac{1}{2}} \mathrm{sgn}(e_1) + {\mu_2}^2 e_1 \end{cases} \tag{35}$$

where μ_1 takes the value of 0 or 1 and $\mu_2 \geq 0$. μ_1 and μ_2 are not equal to 0 at the same time. $\phi_i(e)$ is a nonlinear term.

During $\mu_1 = 1$ and $\mu_2 = 0$, the observer is super twisting. During $\mu_1 = 1$ and $\mu_2 > 0$, GSTO has additional linear terms and extra terms. When the estimation error e_1 is large, $\mu_2 e_1 > \mu_1 |e_1|^{\frac{1}{2}} \mathrm{sgn}(e_1)$ and $\frac{3}{2}\mu_1\mu_2 |e_1| \mathrm{sgn}(e_1) + {\mu_2}^2 e_1 > \frac{{\mu_1}^2}{2} \mathrm{sgn}(e_1)$ are satisfied. Therefore, faster convergence is guaranteed [28].

A structural diagram of GSTO is shown in Fig. 3.

According to (33), the error estimation system can be written as

$$\begin{cases} \dot{e}_1 = -l_1\phi_1(e_1) + e_2 \\ \dot{e}_2 = -l_2\phi_2(e_1) - \dot{D}_\omega. \end{cases} \tag{36}$$

Proof 6: The error state equations of the traditional ESO are

$$\begin{cases} \dot{e}_1 = e_2 - l_1 e_1 \\ \dot{e}_2 = -\dot{D}_\omega - l_2 e_1. \end{cases} \tag{37}$$

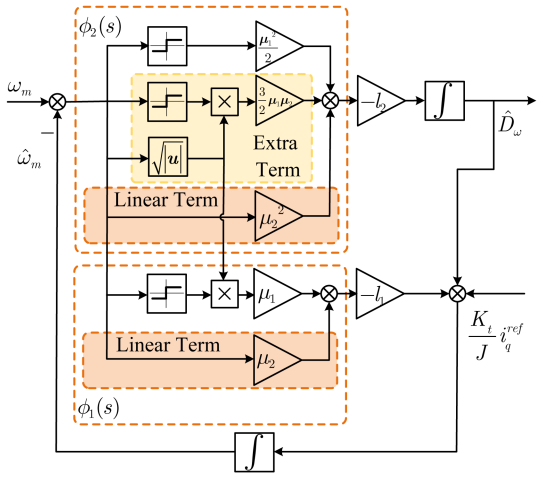

Fig. 3. Structural diagram of the GSTO.

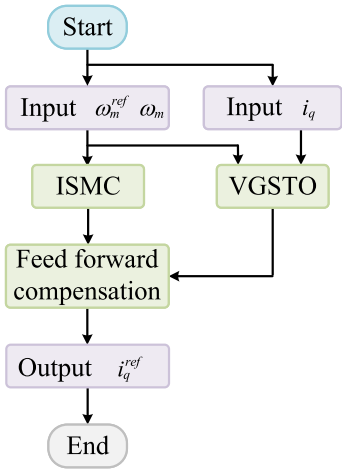

Fig. 4. Structural diagram of the RSCS.

And the error state equations of the observer proposed in this article are

$$\begin{cases} \dot{e}_1 = e_2 - l_1\phi_1(e_1) \\ \dot{e}_2 = -\dot{D}_\omega - l_2\phi_2(e_1) \end{cases} \tag{38}$$

where e_2 represents the total disturbance observation error of the set, and D_ω is the disturbance derivative.

The traditional ESO is subject to the influence of perturbed differentials. Despite the fact that the global asymptotic convergence of the observation error can still be guaranteed, the equilibrium point of this asymptotic convergence will deviate under the impact of perturbed differentials. In other words, the observation error varies in accordance with the changes in the disturbance. When taking into account the dynamics of the observation error, it can be represented as follows:

$$\begin{cases} se_2(s) = -\dot{D}_\omega(s) - \frac{\omega_c^2}{s+\omega_c} e_2(s) \\ e_2(s) = \frac{s+\omega_c}{s^2+\omega_c s+\omega_c^2} - \dot{D}_\omega(s). \end{cases} \tag{39}$$

The observer proposed in this article corrects the deficiencies of the original ESO. Specifically, for the dynamics of e_1, due to the large initial error of e_1, the nonlinear term can provide a faster convergence speed when e_1 is far from the equilibrium point. Moreover, considering that e_1 is the input of the sign function, it is not advisable to adjust further to increase the convergence speed of e_1 near $e_1 = 0$. For the dynamics of e_2, in order to correct the observation error of the original ESO when the disturbance derivative is not zero ($\dot{D}_\omega \neq 0$), the nonlinear term is introduced to correct the influence of the equilibrium point shift caused by $\dot{D}_\omega \neq 0$. At the same time, in order to provide a faster convergence speed.

B. Stability Proof of GSTO

The Lyapunov function is chosen as

$$V_1 = \xi^T C \xi \tag{40}$$

where C is a symmetric and positive definite matrix $\xi^T = \begin{bmatrix} \phi_1(e_1) & e_2 \end{bmatrix}$, and the time derivative of ξ is given by

$$\begin{aligned} \dot{\xi} &= \dot{\phi}_1(e_1) \begin{bmatrix} -l_1\phi_1(e_1) + e_2 \\ -l_2\phi_1(e_1) - \frac{\dot{d}_t}{\dot{\phi}_1(e_1)} \end{bmatrix} \\ &= \dot{\phi}_1(e_1)(A\xi - B\Lambda) \end{aligned} \tag{41}$$

where $\Lambda = \frac{\dot{d}_t}{\dot{\phi}_1(e_1)}$, $A = \begin{bmatrix} -l_1 & 1 \\ -l_2 & 0 \end{bmatrix}$ and $B = \begin{bmatrix} 0 \\ 1 \end{bmatrix}$. Inspired by [29], set $\Delta(\xi,\Lambda) = \begin{bmatrix} \xi \\ \Lambda \end{bmatrix}^T \begin{bmatrix} R & S^T \\ S & -\theta \end{bmatrix} \begin{bmatrix} \xi \\ \Lambda \end{bmatrix}$, where the $\theta \geq 0$. In addition, appropriate R and S matrices are selected to ensure $\Delta(\xi,\Lambda) \geq 0$.

Theorem 1: Let there exist a positive definite symmetric matrix C and a positive constant κ satisfying the following matrix inequality:

$$\begin{bmatrix} A^TC + CA + \kappa C + R & CB + S^T \\ B^TC + S & -\theta \end{bmatrix} \leq 0. \tag{42}$$

System (36) is finite-time stable.

Proof 7: According to (36):

$$\lambda_{\min}\{C\} \|\xi\|_2^2 \leq \xi^T C \xi \leq \lambda_{\max}\{C\} \|\xi\|_2^2 \tag{43}$$

where $\lambda\{C\}$ is the eigenvalue of C, and

$$\|\xi\|_2^2 = {\mu_1}^2 |e_1| + 2\mu_1\mu_2 |e_1|^{\frac{3}{2}} + {\mu_1}^2 {e_1}^2 + {e_2}^2. \tag{44}$$

From (43) and (44) it follows that:

$$|e_1|^{\frac{1}{2}} \leq \frac{\|\xi\|_2}{\mu_1} \leq \frac{{V_1}^{\frac{1}{2}}}{\mu_1 {\lambda_{\min}}^{\frac{1}{2}}\{C\}}. \tag{45}$$

With the help of (41), one has

$$\begin{aligned} \dot{V}_1 &= \dot{\phi}_1(e_1)[\xi^T(A^TC + CA)\xi + \Lambda B^T C\xi + \xi^T CB\Lambda] \\ &= \dot{\phi}_1(e_1) \begin{bmatrix} \xi \\ \Lambda \end{bmatrix}^T \begin{bmatrix} A^TC + CA & CB \\ B^TC & 0 \end{bmatrix} \begin{bmatrix} \xi \\ \Lambda \end{bmatrix} \\ &\leq \dot{\phi}_1(e_1) \left\{ \begin{bmatrix} \xi \\ \Lambda \end{bmatrix}^T \begin{bmatrix} A^TC + CA & CB \\ B^TC & 0 \end{bmatrix} \begin{bmatrix} \xi \\ \Lambda \end{bmatrix} + \Delta(\xi,\Lambda) \right\} \end{aligned}$$

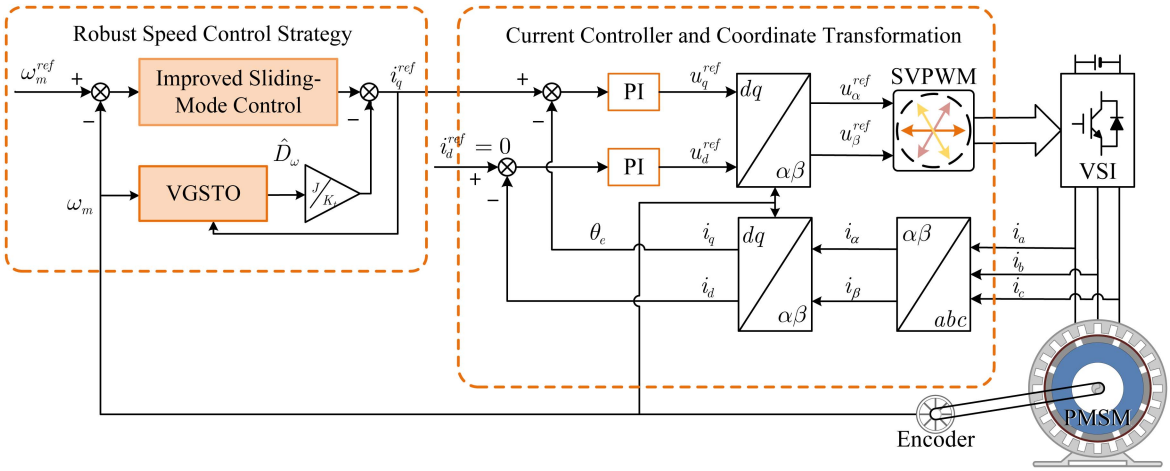

Fig. 5. Block diagram of PMSM regulation system based on the RSCS.

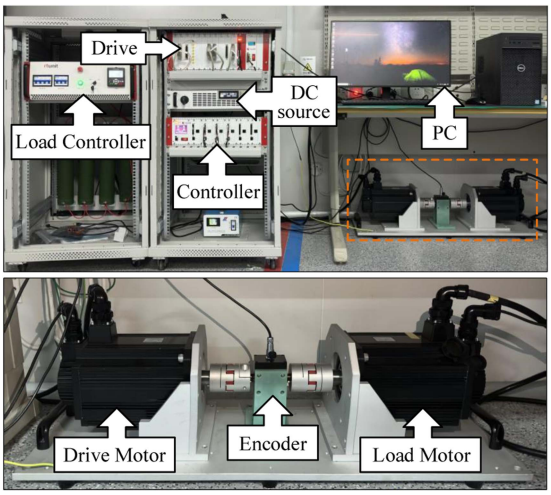

Fig. 6. 2.2 kW-SPMSM towing experimental platform.

$$\leq \dot{\phi}_1(e_1)\begin{bmatrix}\xi\\ \Lambda\end{bmatrix}^T\begin{bmatrix}-\kappa C & 0\\ 0 & 0\end{bmatrix}\begin{bmatrix}\xi\\ \Lambda\end{bmatrix}$$
$$= -\dot{\phi}_1(e_1)\kappa V_1 \tag{46}$$

where $\dot{\phi}_1(e_1) = \frac{1}{2}\mu_1|e_1|^{-\frac{1}{2}} + \mu_2$. It follows from (44):

$$\dot{V}_1 \leq -\frac{\kappa\mu_1{}^2\lambda_{\min}{}^{\frac{1}{2}}\{C\}V^{\frac{1}{2}}}{2} - \kappa\mu_2 V_1. \tag{47}$$

It can be observed that (47) satisfies the finite-time convergence criterion presented in [30]; therefore, the error system in (36) achieves finite-time stability.

C. Introduce variable parameters into the VGSTO

In order to further reduce the dynamic and steady-state observation errors of the observer, the gain μ_2, which was originally a fixed value, is designed as a variable gain

$$\mu_2 = \mu\{\text{sign}[(|\omega_m^{\text{ref}} - \omega_m^{ob}| - \omega_m^{ex})] + 2\}. \tag{48}$$

Among them, μ is the adjustable gain. ω_m^{ref} represents the set rotational speed of the motor, and ω_m^{ob} is the observed value of the observer. These two are fixed parameters and cannot be adjusted. Finally, ω_m^{ex} is the expected limit, which is an adjustable parameter. It is worth noting that (48) represents a bounded function, and the value of μ_2 is bounded. It still satisfies (47), so the finite-time convergence of VGSTO can still be ensured.

The change of parameter μ_2 can be equivalent to the change of the bandwidth gain of the observer, thereby ensuring both the dynamic and steady-state observation performance of the observer [31]. When the difference between the observed value of the observer and the set rotational speed is greater than ω_m^{ex}, $\mu_2 = 3\mu$, the observer will reduce the error of the set rotational speed at a faster convergence rate. When the error drops below ω_m^{ex}, $\mu_2 = \mu$. Since an excessively large value of μ_2 may lead to a large steady-state observation error, the gain switching mentioned above also ensures that the observer will not have an overly large observation error during the steady-state operation.

The control flowchart of the RSCS is shown in Fig. 4.

D. Stability Analysis Of RSCS

Feed-forward compensation of disturbance observation: $\hat{D}_\omega$ at velocity loop controller output According to (32), the compensated velocity loop sliding-mode control law can be obtained as follows:

$$i_q^{ref} = \frac{J}{K_t}(cx_1 + \alpha\{\tanh[\lambda(|s| - a) + 1]\}s^{\frac{q}{p}} + k|s|^{b\cdot\text{sgn}(|s|-1)}s - \hat{D}_\omega). \tag{49}$$

As shown in (49), the observed system disturbances are compensated in the control law in known quantities. When a load disturbance occurs in the system, the controller can respond to the torque change promptly, thus achieving a better disturbance immunity performance without the need for a large control gain.

The stability of the closed-loop control system of the RSCS was analyzed using the Lyapunov stability discriminant theory to demonstrate its stability.

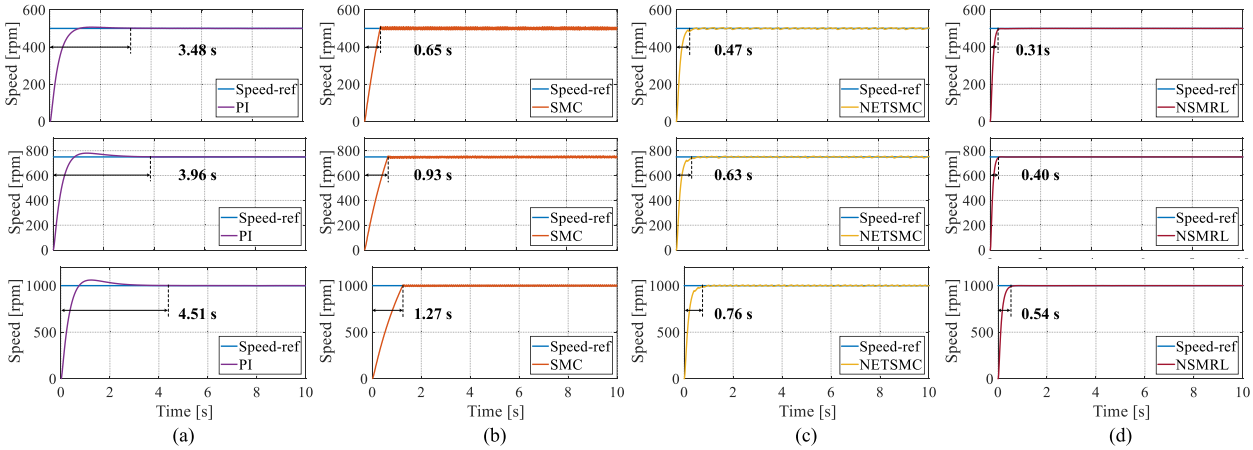

Fig. 7. Tracking performance of four control methods with (500, 750, 1000 r/min) step velocity reference. (a) PI. (b) SMC. (c) NETSMC. (d) NSMRL.

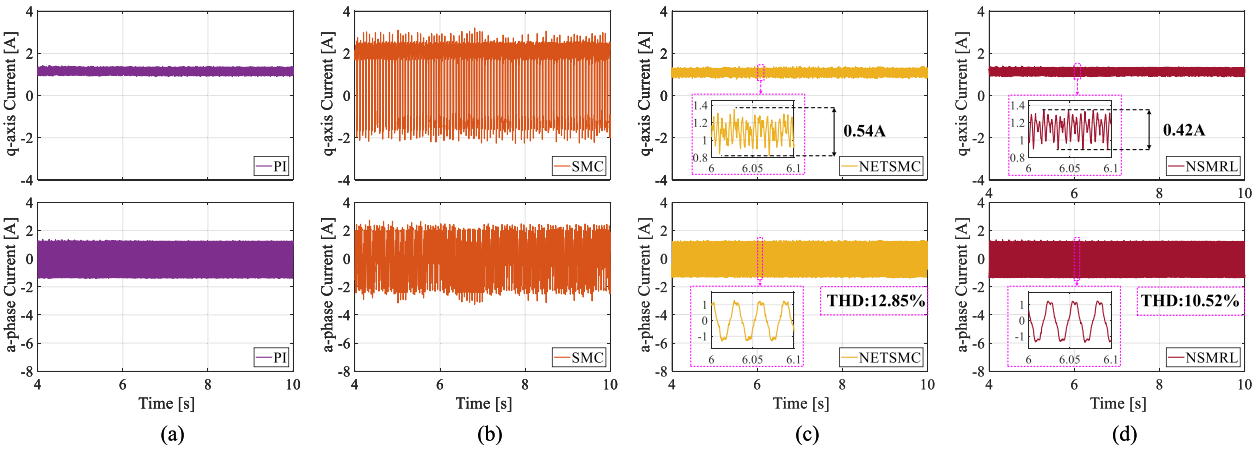

Fig. 8. Performance of steady state phase q-axis current and a-phase current for four control methods under 500 r/min speed reference. (a) PI. (b) SMC. (c) NETSMC. (d) NSMRL.

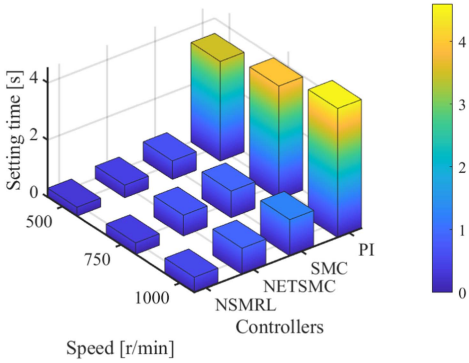

Fig. 9. Comparison of regulation times of four control methods with different step speed references.

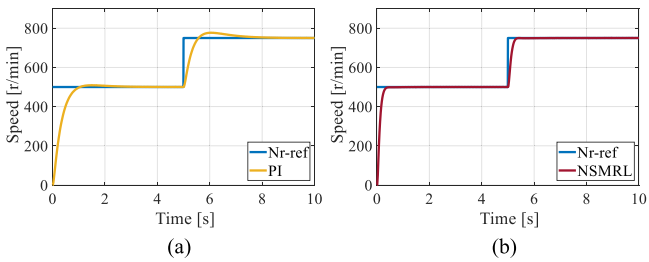

Fig. 10. Performance of two control methods under variable speed reference. (a) PI. (b) NSMRL.

Proof 8: The Lyapunov function is chosen as: $V = \frac{1}{2}s^2$. It can be obtained by combining (27) and (29) that

$$\dot{V} = s\dot{s} = s\left(-\dot{\omega}_m + cx_1\right) = s\left(-\frac{K_t}{J}i_q^{ref} + cx_1 - D_\omega\right). \tag{50}$$

Can be obtained by substituting (47):

$$\dot{V} = -\alpha\left\{\tanh\left[\lambda\left(|s| - a\right)\right] + 1\right\}s^{\frac{q+p}{p}} - k|s|^{b\cdot\mathrm{sgn}(|s|-1)}s^2 + s\left(\hat{D}_\omega - D_\omega\right) \tag{51}$$

where the estimation error of the observer $\hat{D}_\omega - D_\omega$ is bounded, and let the bound on the estimation error take the value d, we have

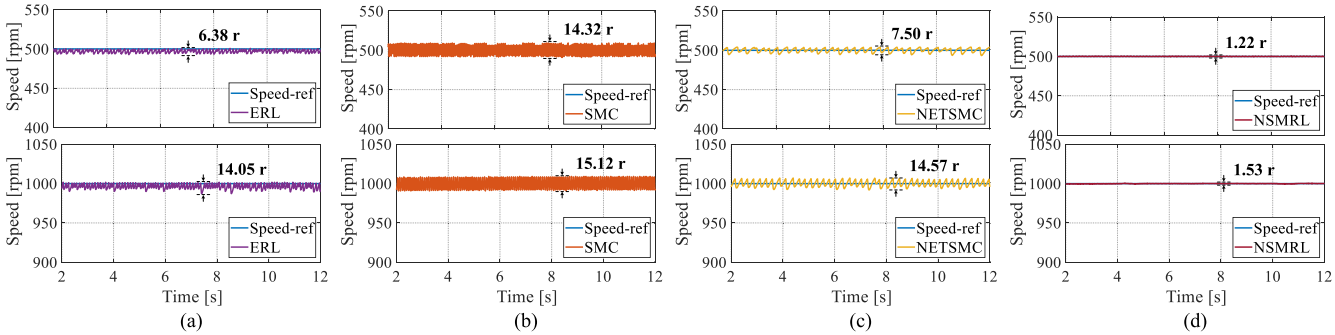

Fig. 11. The fluctuation values of the four control algorithms in the steady-state phase when the set rotational speeds are 500 r/min and 1000 rpm. (a) ERL. (b) SMC. (c) NETSMC. (d) NSMRL.

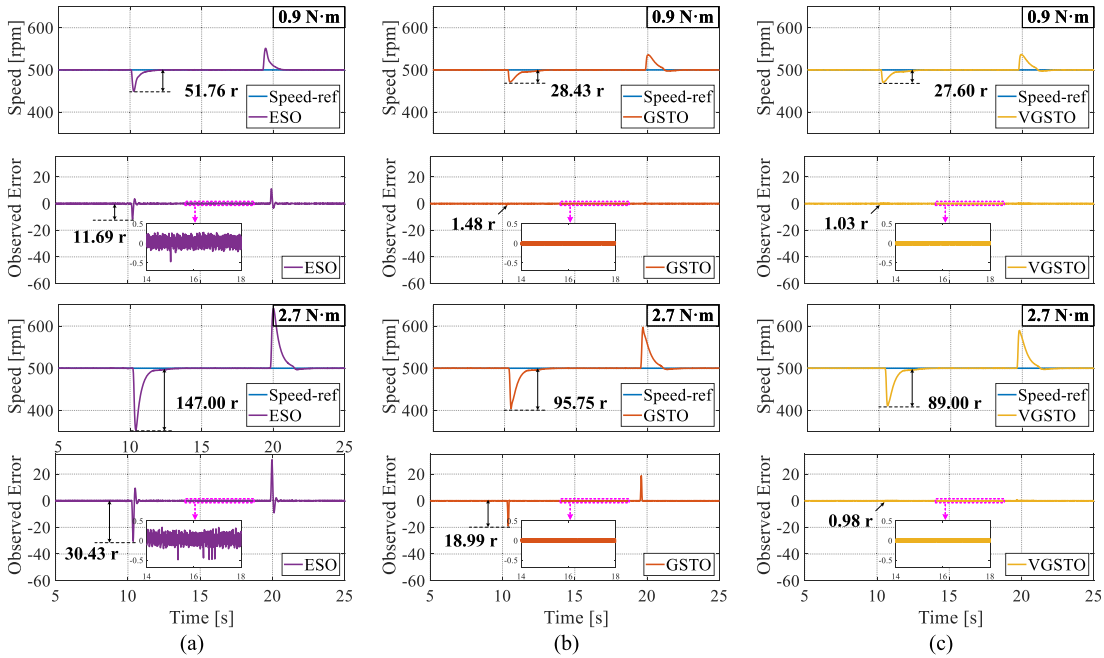

Fig. 12. Rotational speed fluctuation values and observed errors of the three observers under loads of 0.9 N· m and 2.7 N· m. (a) ESO. (b) GSTO. (c) VGSTO.

$|\hat{D}_\omega - D_\omega| \le d$. Simultaneously, both a and k are positive, as are $1 - \mathrm{e}^{-a|s|} > 0$ and $|s|^{\pm b} > 0$. Therefore, it follows from (32) that:

$$\dot{V} \le -\alpha s^{\frac{q+p}{p}} + sd. \tag{52}$$

Taking $\alpha = \alpha_0 + d$, and $s^{\frac{q+p}{p}} > s$ ensure that $\dot{V} \le 0$.

When $\dot{V} \equiv 0$, $s \equiv 0$. A closed-loop control system with a RSCS is asymptotically stable according to the Lyapunov stability theory. A block diagram of the PMSM speed-regulation system is shown in Fig. 5.

The superiority of the transient performance and robustness of the proposed RSCS in a PMSM closed-loop control system was verified. Correlation studies under constant speed, variable speed, and sudden load experimental conditions were carried out on a 2.2 kW-SPMSM experimental platform. The experimental platform included a drive motor, load motor, dc source, motor driver, encoder, PC, load controller, and main controller. The main controller uses a TI TMS320C28346 floating-point processor. A physical diagram of the experimental platform is shown in Fig. 6, in which the dual motor-to-drag loading mode is used; the nominal parameters of the SPMSM are listed in Table I.

TABLE I
PARAMETERS OF PMSM

Parameter	Value and Unit
Number of pole pairs	4
Stator inductance	6.5 mH
Stator resistance	0.12 Ω
Moment of inertia	0.028kg · m^2
Damping factor	0.0048
Permanent-magnet flux linkage	0.18542Wb

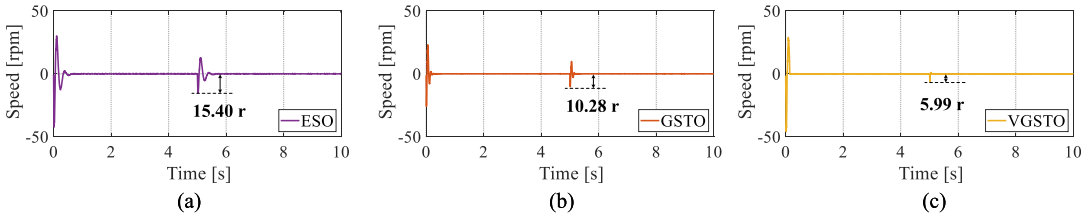

Fig. 13. Observed errors of the three observers under the condition of variable set rotational speeds from 500 to 750 r/min. (a) ESO. (b) GSTO. (c) VGSTO.

VI. Experimental Validation

In this study, an experiment was conducted in two main parts to verify the superiority of the proposed RSCS based on ISMC and VGSTO. First, we compare the transient performance of the NSMRL proposed in this study with that of the conventional PI, SMC, and NETSMC algorithms based on a nonlinear exponential term proposed in [16].

Furthermore, to verify the advantage of the NSMRL proposed in this article in suppressing sliding-mode chattering, the ERL proposed in [32] is introduced. It suppresses the sliding-mode chattering of the system by rewriting the sign function in traditional SMC. A series of experiments were carried out under constant reference speed and variable reference speed conditions with an initial load. In addition, the experimental parameters of the NSMRL presented in this article are as follows: $p = 5$, $q = 3$, $\alpha = 2$, $\lambda = 5$, $a = 1$, $k = 0.3$, $\beta = 0.26$, and $\chi = 30$. To demonstrate the superiority of the observation performance of the VGSTO proposed in this article compared to conventional ESO, a series of sudden load increase and sudden load decrease experiments were performed. In addition, to ensure the fairness of the comparison experiment, the speed loop control algorithm is unified using the NSMRL proposed in this article, choosing the same ω_c as 20. The GSTO parameters are selected as: $\mu_1 = 1$ and $\mu_2 = 1$. The parameters of the VGSTO are selected as: $\mu_1 = 1$, $\mu = 1$, and $\omega_m^{ex} = 5$.

A. Experimental Verification of NSMRL

To ensure fairness of the comparison experiments, for all four groups of experiments, the PI controlled the motor system current loop, and the parameters were kept the same. Fig. 7 shows the speed response results for the four schemes under the step speed reference. When the set rotational speed is 500 r/min, the response times of the four control algorithms are 3.48, 0.65, 0.47, and 0.31 s, respectively. When the set rotational speed is 750 r/min, the response times of the four control algorithms are 3.96, 0.93, 0.63, and 0.40 s, respectively. When the set rotational speed is 1000 r/min, the response times of the four control algorithms are 4.51, 1.27, 0.76, and 0.54 s, respectively. It can be seen that the NSMRL control algorithm proposed in this article has the shortest response time. Fig. 8 shows the current performance of the four control methods in the steady state phase of the system at a step speed of 500 r/min. It is clear that the q-axis current of the proposed NSMRL exhibits less fluctuation, and the a-phase current is smoother than that of the NETSMC. The THD value of the a-phase current of the NSMRL is also smaller. The fastness values of the four control methods are compared in Fig. 9. It can be clearly seen that the NSMRL proposed in this article has advantages in terms of rapidity.

Fig. 10 shows the response to PI and NSMRL speed tracking under variable speed conditions, indicating that NSMRL has good speed and no overshooting of the response under variable speed conditions.

In order to further demonstrate the advantages of NSMRL in terms of sliding-mode chattering, a comparison was conducted in the steady-state phase under experimental conditions of set rotational speeds of 500 r/min and 1000 r/min, as shown in Fig. 11. When the set rotational speed is 500 r/min, the peak values of chattering in the steady state of the four control algorithms are 3.48, 14.32, 7.50 and 1.22 r, respectively. When the set rotational speed is 1000 r/min, the peak values of chattering in the steady state of the four control algorithms are 14.05, 15.12, 14.57, and 1.53 r, respectively. It can be seen that the chattering of the NSMRL proposed in this article is smaller than that of ERL, SMC, and NETSMC.

B. Experimental Verification of VGSTO

In order to demonstrate the superiority of the VGSTO proposed in this study, we applied and unloaded the same magnitude of load at the same time during the experimental process. A comprehensive comparison was carried out in terms of disturbance rejection performance and observation performance (including the speed observation performance in dynamic and steady states, as well as the ability to observe the load).

Fig. 12 shows the peak values of speed fluctuations and the dynamic and steady-state observation errors under the action of three observers when the loads are 0.9 and 2.7 N· m. It can be seen that compared with the ESO, the GSTO has smaller peak values of speed fluctuations and better speed observation performance in both dynamic and steady states under the action of the two loads. At the same time, the addition of variable parameters enables the VGSTO to have smaller peak values of speed fluctuations and better performance in terms of dynamic speed observation errors.

Fig. 13 shows the observation errors of the three observers under the variable speed setting condition where the set rotational speed changes from 500 to 750 r/min. The observation errors of the three observers during the speed change are 15.40, 10.28, and 5.99 r, respectively. Compared with the ESO and GSTO, the VGSTO has smaller observation errors and shorter adjustment time, demonstrating the strongest performance in terms of dynamic speed observation error.

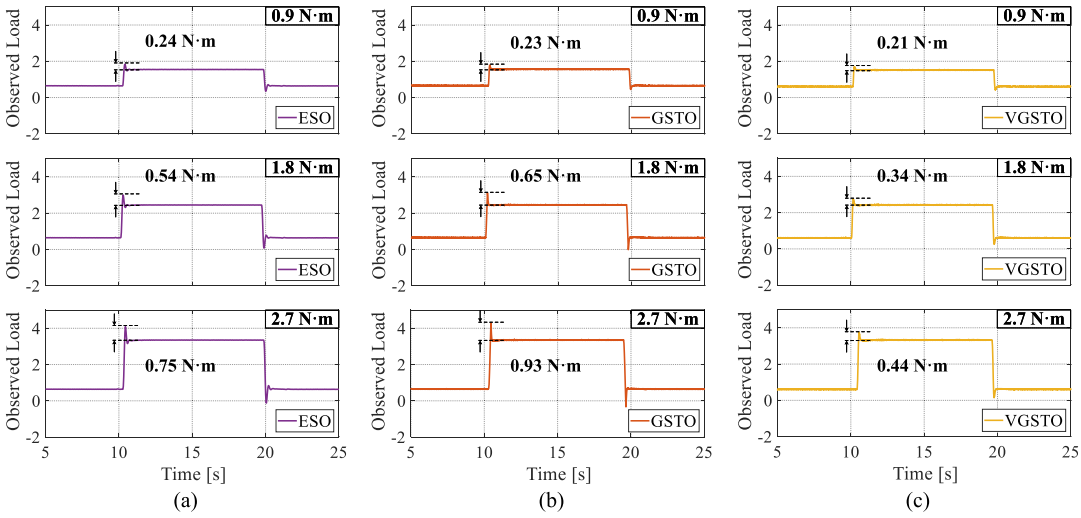

Fig. 14. Load observation situations of the three observers under three different load conditions. (a) ESO. (b) GSTO. (c) VGSTO.

Finally, as we can see from Fig. 14, as the applied load increases, the observation errors of the three observers in observing the load will also increase. Compared with the traditional ESO, the GSTO has a shorter adjustment time when observing the load, but the peak value of the observation error it causes will increase. The VGSTO effectively solves the above contradiction. It not only achieves a shorter adjustment time, but also has the smallest peak value of the observation error, demonstrating excellent ability in observing the load.

VII. Conclusion

To improve the performance of a permanent magnet synchronous motor speed control system, an NSMRL is proposed, which has a faster convergence speed and suppresses sliding-mode chattering compared to the traditional exponential reaching law and other reaching laws in the literature that use nonlinear exponential terms. Based on NSMRL, ISMC is designed and VGSTO, which introduces linear and extra terms, has better observation performance and is superior to the traditional ESO. Finally, VGSTO solves ESO's problem by not selecting an observer bandwidth that is too large because it is affected by considering the high-frequency noise and the stiffness of the system. The superiority of the proposed RSCS (ISMC+VGSTO) method was experimentally verified, and the results show that the proposed method can achieve satisfactory performance with a fast transient response and strong anti-interference ability.

References

[1] M. Shao, Y. Deng, H. Li, J. Liu, and Q. Fei, "Robust speed control for permanent magnet synchronous motors using a generalized predictive controller with a high-order terminal sliding-mode observer," *IEEE Access*, vol. 7, pp. 121540–121551, 2019.

[2] H. Cao, Y. Deng, Y. Zuo, X. Liu, J. Wang, and C. H. T. Lee, "A variable structure ADRC for enhanced disturbance rejection and improved noise suppression of PMSM speed system," *IEEE Trans. Ind. Electron.*, vol. 72, no. 5, pp. 4481–4495, May 2025.

[3] H. Cao et al., "Improved deadbeat predictive current control of PMSM drives with repetitive control-based disturbance correction observer," *IEEE Trans. Power Electron.*, vol. 40, no. 1, pp. 801–812, Jan. 2025.

[4] W. Zou, T. Shi, J. Guo, and Z. Xiang, "A novel adaptive fuzzy control scheme for a class of nonlinear planar systems under state constraints," *IEEE Trans. Circuits Syst. II: Exp. Briefs*, vol. 71, no. 2, pp. 827–831, Feb. 2024.

[5] H. Li, S. Wang, Y. Xie, S. Zheng, and P. Shi, "Virtual reference-based fuzzy noncascade speed control for PMSM systems with unmatched disturbances and current constraints," *IEEE Trans. Fuzzy Syst.*, vol. 31, no. 12, pp. 4249–4261, Dec. 2023.

[6] B. Wang, M. Tian, Y. Yu, Q. Dong, and D. Xu, "Enhanced ADRC with quasi-resonant control for PMSM speed regulation considering aperiodic and periodic disturbances," *IEEE Trans. Transport. Electrific.*, vol. 8, no. 3, pp. 3568–3577, Sep. 2022.

[7] T. T. Nguyen, H. N. Tran, T. H. Nguyen, and J. W. Jeon, "Recurrent neural network-based robust adaptive model predictive speed control for PMSM with parameter mismatch," *IEEE Trans. Ind. Electron.*, vol. 70, no. 6, pp. 6219–6228, Jun. 2023.

[8] H. Cao, Y. Deng, C. Zhao, Y. Shen, X. Liu, and C. H. T. Lee, "Enhanced position estimation accuracy based on improved super-twisting observer and position compensation PLL for PMSM sensorless control," *IEEE Trans. Circuits Syst. II: Express Brief.*, vol. 72, no. 2, pp. 414–418, Feb. 2025.

[9] P. Gao, G. Zhang, H. Ouyang, and L. Mei, "An adaptive super twisting nonlinear fractional order PID sliding mode control of permanent magnet synchronous motor speed regulation system based on extended state observer," *IEEE Access*, vol. 8, pp. 53498–53510, 2020.

[10] X. Zhang, L. Sun, K. Zhao, and L. Sun, "Nonlinear speed control for PMSM system using sliding-mode control and disturbance compensation techniques," *IEEE Trans. Power Electron.*, vol. 28, no. 3, pp. 1358–1365, Mar. 2013.

[11] L. Chen et al., "Sensorless fixed-time sliding mode control of PMSM based on barrier function adaptive super-twisting observer," *IEEE Trans. Power Electron.*, vol. 39, no. 3, pp. 3037–3051, Mar. 2024.

[12] Y. Zuo, C. Lai, and K. L. V. Iyer, "A review of sliding mode observer based sensorless control methods for PMSM drive," *IEEE Trans. Power Electron.*, vol. 38, no. 9, pp. 11352–11367, Sep. 2023.

[13] J. P. Mishra, X. Yu, M. Jalili, and Y. Feng, "On fast terminal sliding-mode control design for higher order systems," in *Proc. IECON 42nd Annu. Conf. IEEE Ind. Electron. Soc.*, Florence, Italy, 2016, pp. 252–257.

[14] G. Sun, Z. Ma, and J. Yu, "Discrete-time fractional order terminal sliding mode tracking control for linear motor," *IEEE Trans. Ind. Electron.*, vol. 65, no. 4, pp. 3386–3394, Apr. 2018.

[15] F. Bodur and O. Kaplan, "A novel sliding mode control based on super twisting reaching law for PMSM speed controller with fixed-time disturbance observer," in *Proc. 12th Int. Conf. Renewable Energy Res. Appl.*, Oshawa, ON, Canada, 2023, pp. 1–6.

[16] Y. Wang, Y. Feng, X. Zhang, and J. Liang, "A new reaching law for anti-disturbance sliding-mode control of PMSM speed regulation system," *IEEE Trans. Power Electron.*, vol. 35, no. 4, pp. 4117–4126, Apr. 2020.
[17] X. Liu, Y. Deng, J. Wang, H. Li, and H. Cao, "Fixed-time generalized active disturbance rejection with quasi-resonant control for PMSM speed disturbances suppression," *IEEE Trans. Power Electron.*, vol. 39, no. 6, pp. 6903–6918, Jun. 2024.
[18] Y. Li, Y. Hu, X. Ma, and L. Liu, "Sensorless control of dual three-phase IPMSM based on frequency adaptive linear extended state observer," *IEEE Trans. Power Electron.*, vol. 38, no. 11, pp. 14492–14503, Nov. 2023.
[19] Z. Pan, X. Wang, T. T. G. Hoang, Z. Wang, and L. Tian, "DC-link voltage disturbance rejection strategy of pwm rectifiers based on reduced-order LESO," *IEEE Access*, vol. 7, pp. 103693–103705, 2019.
[20] H. Liu and S. Li, "Speed control for PMSM servo system using predictive functional control andextended state observer," *IEEE Trans. Ind. Electron.*,vol. 59, no. 2, pp. 1171–1183, Feb. 2012.
[21] J. Han, "From PID to active disturbance rejection control," *IEEE Trans. Ind. Electron.*, vol. 56, no. 3, pp. 900–906, Mar. 2009.
[22] Q. Hou et al., "High-order NESO based enhanced adrc for PMSM drives considering uncertainty and measurement noise suppression," in *Proc. IECON 48th Annu. Conf. IEEE Ind. Electron. Soc.*, Brussels, Belgium, 2022, pp. 1–6.
[23] L. Zhao, B. Zhang, H. Yang, and Y. Wang, "Observer-based integral sliding mode tracking control for a pneumatic cylinder with varying loads," *IEEE Trans. Syst., Man, Cybern. Syst.*, vol. 50, no. 7, pp. 2650–2658, Jul. 2020.
[24] Q. Hou et al., "Super-twisting extended state observer-based quasi-proportional-resonant controller for permanent magnet synchronous motor drive system," *IEEE Trans. Transport. Electrific.*, vol. 10, no. 1, pp. 1596–1604, Mar. 2024.
[25] H. Wang, Y. Deng, M. Shao, H. Cao, X. Liu, and X. Zhou, "A novel state restriction and disturbance suppression strategy based on variable gain dynamic manifold super-twisting sliding mode control," in *Proc. IEEE 10th Int. Power Electron. Motion Control Conf.*, Chengdu, China, 2024, pp. 2384–2389.
[26] L. Yang, L. Liu, and J. Zhang, "A bi-bandwidth extended state observer for a system with measurement noise and its application to aircraft with abrupt structural damage," *Aerosp. Sci. Technol.*, vol. 114, Jul. 2021, Art. no. 106742.
[27] V. Utkin and J. Shi, "Integral sliding mode in systems operating under uncertainty conditions," in *Proc. 35th IEEE Conf. Decis. Control*, Kobe, Japan, 1996, pp. 4591-4596.
[28] J. A. Moreno, "A linear framework for the robust stability analysis of a Generalized Super-Twisting Algorithm," in *Proc. 6th Int. Conf. Elect. Eng., Comput. Sci. Autom. Control*, Toluca, Mexico, 2009, pp. 1–6.
[29] L. Zhao, S. Gu, J. Zhang, and S. Li, "Finite-time trajectory tracking control for rodless pneumatic cylinder systems with disturbances," *IEEE Trans. Ind. Electron.*, vol. 69, no. 4, pp. 4137–4147, Apr. 2022.
[30] S. Yu, X. Yu, B. Shirinzadeh, and Z. Man, "Continuous finite-time control for robotic manipulators with terminal sliding mode," *Automatica*, vol. 41, no. 11, pp. 1957–1964, Nov. 2005.
[31] S. Zhu et al., "Robust speed control of electrical drives with reduced ripple using adaptive switching high-order extended state observer," *IEEE Trans. Power Electron.*, vol. 37, no. 2, pp. 2009–2020, Feb. 2022.
[32] H. Komurcugil, S. Bayhan, N. Guler, and H. Abu-Rub, "A new exponential reaching law approach to the sliding mode control: A multilevel multifunction converter application," *IEEE Trans. Ind. Electron.*, vol. 70, no. 8, pp. 7557–7568, Aug. 2023.

Yifan Xu (Graduate Student Member, IEEE) was born in Weihai City, Shandong Province, China, in 2000. He received the B.E. degree from the Yantai University, Shandong, China, in 2022. He is currently working toward the Ph.D. degree in mechatronic engineering with the University of Chinese Academy of Sciences, Beijing, China, and the Changchun Institute of Optics, Fine Mechanics and Physics, Chinese Academy of Sciences, Changchun, China.

His research interests include advanced control theories for motor drive systems, such as sliding-mode control and active disturbance rejection control.

Bin Zhang (Member, IEEE) was born in Jilin Province, China, in 1981. He received the B.E. degree in automation from the Dalian University of Technology, Dalian, China, in 2004, and the Ph.D. degree in mechatronic engineering from the Changchun Institute of Optics, Fine Mechanics and Physics, Chinese Academy of Sciences, Changchun China, in 2010.

He is currently a Professor with the Changchun Institute of Optics, Fine Mechanics and Physics, Chinese Academy of Sciences. His research interests include telescope servo system and active optics control system.

Yongting Deng (Senior Member, IEEE) was born in Shandong, China, in 1987. He received the B.E. degree in automation from the China University of Petroleum (East China), Qingdao, China, in 2010, and the M.S. degree in mechatronic engineering and the Ph.D. degree in mechatronic engineering from the Changchun Institute of Optics, Fine Mechanics and Physics, Chinese Academy of Sciences, Changchun, China, in 2015.

He is currently a Professor with the Changchun Institute of Optics, Fine Mechanics and Physics, Chinese Academy of Sciences. He has authored or coauthored more than 70 publications in the research interests that include controller design for ac motor drives and linear motor drives, intelligent control, and high-precision machine control techniques.

Yuxin Kang (Graduate Student Member, IEEE) was born in Shanxi, China, in 1997. He received the B.E. degree in applied physics from the Taiyuan University of Technology, Shanxi, China, in 2020. He is currently working toward the Ph.D. degree in mechatronic engineering with the University of Chinese Academy of Sciences, Beijing, China, and the Changchun Institute of Optics, Fine Mechanics and Physics, Chinese Academy of Sciences, Changchun, China.

His main research interests include advanced control theories and applications on motor drive systems.

Xiufeng Liu (Member, IEEE) was born in Changchun, China, in 1998. He received the B.E. degree in vehicle engineering from the Changchun University of Technology, Changchun, China, in 2020, and the M.S. and Ph.D. degrees in mechatronic engineering from the Changchun Institute of Optics, Fine Mechanics and Physics, Chinese Academy of Sciences, Changchun, in 2025.

He is currently an Assistant Professor with the Changchun Institute of Optics, Fine Mechanics and Physics, Chinese Academy of Sciences. His research interests include advanced PMSM control algorithms, such as fixed-time control, sliding mode control, and active disturbance rejection control.

Haiyang Cao (Member,IEEE) was born in Shandong, China, in 1997. He received the Ph.D. degree in mechatronic engineering from the University of Chinese Academy of Sciences, Beijing, China, and the Changchun Institute of Optics, Fine Mechanics and Physics, Chinese Academy of Sciences, Changchun, China, in 2025.

Currently, he is a Postdoctoral Researcher with the Ningbo Institute of Materials Technology and Engineering, Chinese Academy of Sciences, Ningbo, China. From 2023 to 2024, he was a Visiting Researcher with the School of Electrical and Electronic Engineering, Nanyang Technological University, Singapore. His research interests include electric machines and drives, and advanced control strategies.